Chaos
An Interdisciplinary Journal of Nonlinear Science

RESEARCH ARTICLE | APRIL 18 2025

Secondary shearless bifurcations for two isochronous resonant perturbations

B. B. Leal ; M. J. Lazarotto ; M. Mugnaine ; A. M. Ozorio de Almeida ; R. L. Viana ; I. L. Caldas

Chaos 35, 043136 (2025)
https://doi.org/10.1063/5.0233732

Secondary shearless bifurcations for two isochronous resonant perturbations

Cite as: Chaos 35, 043136 (2025); doi: 10.1063/5.0233732
Submitted: 16 August 2024 · Accepted: 22 January 2025 ·
Published Online: 18 April 2025

View Online Export Citation CrossMark

B. B. Leal,[1] M. J. Lazarotto,[1] M. Mugnaine,[1,a)] A. M. Ozorio de Almeida,[2] R. L. Viana,[3,4] and I. L. Caldas[1]

AFFILIATIONS

[1]Institute of Physics, University of São Paulo, 05508-900 São Paulo, SP, Brazil
[2]Brazilian Center for Research in Physics, Rio de Janeiro, RJ 22290-180, Brazil
[3]Department of Physics, Federal University of Paraná, Curitiba, PR 81531-980, Brazil
[4]Interdisciplinary Center for Science, Technology, and Innovation, Curitiba, PR 81530-000, Brazil

[a)]**Author to whom correspondence should be addressed:** mmugnaine@gmail.com

ABSTRACT

Shearless curves are characteristic of nontwist systems and are not expected to exist in twist systems. However, the appearance of secondary shearless curves in the central area of islands has been reported in a few studies where the twist condition is still satisfied. In addition to these studies, we present a scenario in which secondary shearless curves emerge when two independent resonances interact on the same resonant surface. By varying the magnitude of the perturbation parameters, we observe the emergence of multiple secondary shearless curves, which can appear in pairs or individually. Our results are obtained for two discrete systems—the two-harmonic standard map and the Ullmann map—as well as for the Walker–Ford Hamiltonian flow.

Transport, in dynamical systems, is defined as the collective motion of many chaotic trajectories through the phase space. Regular trajectories can act as partial or total barriers, leading to a scenario of low or null transport, respectively. One example of a robust barrier is the shearless curve, a special solution for nontwist systems. Interestingly, such solutions can be found locally in twist systems, especially when there is a resonant mode coupling. In this work, we explore the possibility of local shearless curves in three different conservative systems. We find that shearless curves can emerge in pairs or alone, depending on the bifurcation of the periodic points that they surround. The same scenario is observed in all systems studied, indicating that local shearless curves are a recurrent phenomenon in conservative twist systems.

I. INTRODUCTION

Non-integrable Hamiltonian systems are known for the coexistence of regular and chaotic solutions in the phase space. Due to the complexity involving the mixing of solutions that have different characteristics, chaotic trajectories in phase space can be partially or totally restricted by regular structures that act as barriers, leading to non-ergodic chaotic motion.[1] Area-preserving maps are useful tools for analyzing the behavior of these Hamiltonian systems. They can be specified by analytical formulas or numerically obtained as Poincaré sections of successive intersections of Hamiltonian flows.[2]

Among conservative maps, we highlight the class of *twist maps*, consisting of maps with variational formulation that can be derived from generating functions.[3] The twist maps are known for satisfying the twist condition; i.e., in an angle-action portrait, as we vary the action, the iterated points will lie on different concentric circles with different time averages of the angle of rotation. However, it is possible to introduce area-preserving maps with non-monotonic functions. These maps are called *nontwist* since the twist condition is violated at some point in phase space. A great analysis of the rotation number for nontwist maps was performed in Ref. 4.

The time average rotation, represented by the rotation number, depends on the action.[5] Taking trajectories along a radial line from the equilibrium point, we can compute the rotation number as a function of distance along this line. In the case of an integrable system, the average angle coincides with the average angle variable. Alternatively, the rotation number can be defined as the average jump per iteration with respect to a given equilibrium point.[6] For twist maps, this average is always monotonic.

Due to the violation of the twist condition (named a non-degeneracy condition for Hamiltonian continuum systems), different dynamical phenomena emerge in the phase space.[6,7] Twin island chains and separatrix reconnection are examples of nontwist phenomena that occur because of the non-monotonicity of the rotation number.[8,9] The solution in which the twist condition fails is called a shearless/twistless curve since the derivative (frequently called the shear/twist) of the rotation number with respect to the action vanishes at such a curve.[6] The definition of a shearless curve by the zero derivative of the rotation number by the radial distance coincides with the zero derivative of the average rotation number by the action variable, in the case of an integrable system. These shearless curves are called "primary" or principal.

In general, an invariant curve can be regarded as a transport barrier.[10] However, in twist maps, due to the KAM theorem, these barriers are progressively destroyed as the perturbation strength is continuously increased. Shearless curves, on the other hand, are robust in the sense that they can survive the destruction of invariant curves on both sides with respect to the action variable. We shall use the word "transport barrier" for the shearless curves corresponding to local extrema of the rotation number profile.

The presence of shearless curves was identified in many physical systems, such as the Rossby wave experiments in a rotating annular tank,[11,12] in toroidal devices for plasma confinement, such as the TCABR[13,14] tokamak and Texas Helimak,[15] in mathematical models for Rossby waves in shear flows,[7] magnetically confined plasmas,[16] zonal flows in geophysical systems, and chaotic advection,[17,18] to cite some examples.

The twist measures the rate of change of frequencies over different invariant curves,[9] and for twist (nontwist) maps, its sign is constant (changes). In the action-angle description, these invariant circles are centered in the origin and the rotation number is a global measure since it is related to the rotation of the points around its center.[5] However, it is possible to define the rotation number value for points rotating around any fixed point in phase space. Therefore, the concept of an *internal rotation number* was proposed as the measure of torsion of each torus with respect to its elliptic point (center of the island).[19–21]

Along with the idea of an internal rotation number, the possibility of shearless (twistless) curves was also demonstrated in twist maps. In this case, the shearless curve is related to an extreme value for the internal rotation number, and since it is related to an inner structure of the phase space, *e.g.*, an island, it is called a secondary shearless curve. Dullin *et al.*[19] observed the existence of twistless curves in the neighborhood of an elliptic point that goes through a tripling bifurcation. Abud and Caldas[20] also identified these twistless curves in the standard twist map in the neighborhood of tripling and quadrupling bifurcations. They also observed such curves in twist maps for field lines in tokamaks.[21]

According to Dullin, Meiss, and Sterling, the presence of a shearless curve in the neighborhood of a periodic orbit that goes through a tripling bifurcation is generic, and the authors also affirm that the twist of an orbit can be forced to be zero if there is a sufficient number of parameters.[19] Interestingly, secondary shearless curves were also identified in models of optical lattices[22] and of large aspect ratio tokamaks with ergodic limiter.[23] With these results, we suspect that secondary shearless curves are more common than initially assumed. In order to investigate the generality of secondary shearless curves, we propose studying a series of dynamical systems to verify the possibility of these curves around different types of bifurcations.

In this paper, we study the emergence of secondary shearless curves in three different twist systems. Our investigations are based on the computation of the internal rotation number profile and phase space analysis of the extreme points in the profile and the emergence of shearless curves around elliptic points.

The first system is a two-parameter twist map, known as the two-harmonic standard map, presented in Ref. 24, formed by the addition of a second resonant perturbation in the generic version of the standard map. This map can be considered a model for the competition of different resonant modes where the resulting *isochronous islands* go through different bifurcations, such as pitchfork and saddle-node. Isochronous islands are distinct islands with the same frequency and rotation number, and they emerge as a consequence of multiple resonant perturbations acting in the same resonant surfaces (curves). The second system is presented in Ref. 23, a magnetic field line map, adapted from the Ulmann map,[25] composed of two parts: the first dictating the evolution of the field lines between two coils of the ergodic limiter and the second that describes the action of the limiter as an impulsive perturbation. The last system studied is the well-established Walker–Ford Hamiltonian flow,[26] which describes the effect of resonances on the appearance of isochronous island chains.

The present paper is organized as follows. Section II is dedicated to the investigations around the two-harmonic standard map, the simplest analyzed system, which will give us a clearer explanation of the emergence of secondary shearless tori. In Sec. III, we present the results on the modified Ulmann map and the impact of different arrangements of resonant modes on the rise of shearless curves. The results on the Walker–Ford Hamiltonian flow are presented in Sec. III, where, in contrast to Secs. II and II, we study the emergence of a shearless tori in the time-continuous system. Our conclusions are presented in Sec. V.

II. TWO-HARMONIC STANDARD MAP AND LOCAL SHEARLESS TORI

The two-harmonic standard map, also called a standard map with two modes, is defined by the equations[24]

$$y_{n+1} = y_n - \frac{K_1}{2\pi m_1}\sin(2\pi m_1 x_n) - \frac{K_2}{2\pi m_2}\sin(2\pi m_2 x_n),$$
$$x_{n+1} = x_n + y_{n+1}, \tag{1}$$

where x and y are taken mod 1, K_1 and K_2 are the perturbation amplitudes, and m_1 and m_2 are the modes of the resonant perturbations. Here, we consider $K_1, K_2 \in \mathbb{R}^*_+$ and $m_1, m_2 \in \mathbb{N}$. The two-harmonic map is a generalization of the extended standard map (ESM), where $m_1 = 1$ and $m_2 = 2$. The ESM arises in the study of a one-dimensional lattice of particles that interact elastically with their nearest neighbors.[27,28]

The map (1) was proposed as a model for the competition between two resonant modes, m_1 and m_2.[24] The two resonant perturbations generate different numbers of islands in the same region

of the phase space, depending on the parameters.[29] As investigated in Ref. 24, the number of isochronous islands along the line $y = 0$ is equal to the mode number of the corresponding resonant term. Thus, if we observe m_1 (m_2) islands at $y = 0$ in the phase space of map (1), we say that the mode m_1 (m_2) is predominant. The transitions from the chain of islands associated with the mode m_1 to the chain of islands of the second mode m_2 can occur either directly or via intermediate modes. For more information about the transition routes, see Ref. 24.

The islands along the line $y = 0$ exhibit a period and frequency equal to unity for both modes m_1 and m_2. The global winding number is defined by the limit

$$\omega = \lim_{n\to\infty} \frac{x_n - x_0}{n}, \tag{2}$$

and it is also equal to unity for these islands. The two resonant perturbations can act in the same winding number surface, and the number of chains of islands in this surface varies according to the perturbation parameters $m_{1,2}$ and $K_{1,2}$. It is worth noting that to determine (2), x_n must be computed without applying the modulo operation.

The standard map is a twist map; *i.e.*, it satisfies the twist condition $\frac{\partial x_{n+1}}{\partial y_n} \neq 0$ for every point in the phase space. As a consequence, if we compute the winding number profile for different orbits with initial conditions on a fixed line x, the value of ω changes monotonically with y and forms a plateau in regions where there are islands. The addition of a second resonant perturbation to the standard map does not alter the twist property of the system, and the winding number profile remains monotonic. However, non-monotonic profiles can be obtained if we compute the rotation number locally by measuring the rotation of a single island with respect to its elliptic point.[20,23,30] Thus, we can define an internal rotation number ω_{in}, which is computed by the equation[20]

$$\omega_{in} = \lim_{n\to\infty} \frac{1}{2\pi n} \sum_{n=1}^{\infty} P_n \hat{\theta} P_{n+1}, \tag{3}$$

with $\theta = P_n \hat{\theta} P_{n+1}$ being the angle between two consecutive points in the phase space. A schematic illustration of the computation of ω_{in} is shown in Fig. 1. Due to the normalization by 2π, the internal rotation number is in the range $[0, 1]$. Just as for the global counterpart ω, a rational value of ω_{in} indicates a periodic orbit, whereas an irrational value corresponds to a quasiperiodic orbit. The internal rotation number also does not converge for chaotic solutions.

The non-monotonicity of the internal winding number is characterized by an extreme in its profile, and such a point refers to the local shearless curve, also called a twistless torus.[19,20,23,30] Shear, or twist, is related to the derivative of the rotation number with respect to the action,[19] so at an extremum of ω_{in}, we have $\omega'_{in} = 0$, indicating the absence of shear or twist.

The equations in (1) are a simple model for twist Hamiltonian systems with multiple resonant perturbations. Following the analysis performed in Ref. 23, we investigate the existence of twistless tori for different combinations of modes m_1 and m_2 and in different transition routes discussed in Ref. 24.

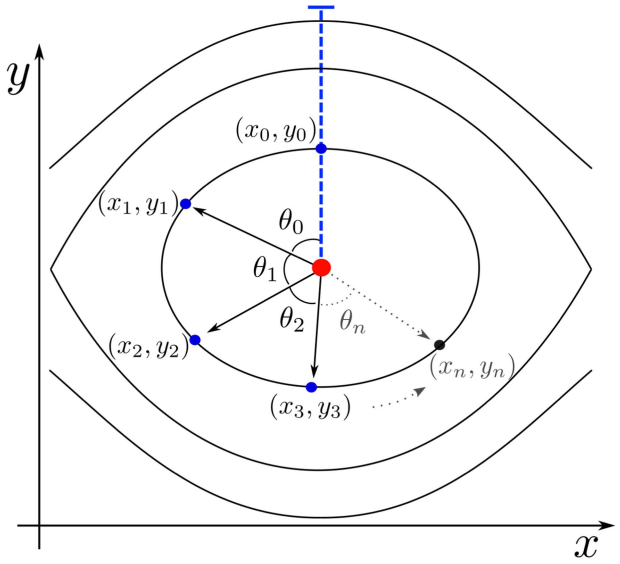

FIG. 1. Schematic figure for the calculation of ω_{in}. For an initial point (x_0, y_0) over the winding profile reference line (dashed blue line), the inner angle θ_n is sequentially evaluated relative to the center of the island.

A. Emergence of one shearless curve

As shown in Ref. 24, one of the possible transitions from one island chain to the other is via a pitchfork bifurcation. As an example, we take the transition $m_1 = 2 \to m_2 = 3$, where the elliptic point at $(x, y) = (0.5, 0)$ goes through a pitchfork bifurcation. During this process, it is replaced by a hyperbolic point, and other two new elliptic points emerge. This transition is presented in Fig. 2. Along with the phase spaces, we computed the internal winding number for each island in the phase space relative to their corresponding elliptic points. The profiles are also presented in Fig. 2.

As shown in Fig. 2, as the value of K_2 increases, the island of period one centered on the point $(x, y) = (0.5, 0)$ changes its form, as seen when comparing panels (a) and (b). The shape of the island around the point $(x, y) = (0, 0)$ remains the same. Further increasing K_2 results in the phase space depicted in Fig. 2(c), where a pitchfork bifurcation occurs and a hyperbolic point replaces the stable point and two new elliptic points emerge along the line at $y = 0$. In this case, the transition from mode m_1 to m_2 occurs through a single pitchfork bifurcation.

The internal winding number profiles presented in Figs. 2(d)–2(f) were calculated with 5.10^3 initial conditions distributed along the blue and black lines in the phase space and iterated for 10^4 iterations. If the limit (3) converges, the corresponding value of ω_{in} is plotted for the respective value of y. In Fig. 2(d), we observed that both profiles have monotonic behavior that decreases as the value of y increases; thus, no internal shearless torus is present in the phase space. A similar behavior is observed for the island centered at $(x = 0, y = 0)$ for greater values of K_2, as shown by the blue curves in Fig. 2(e) and 2(f).

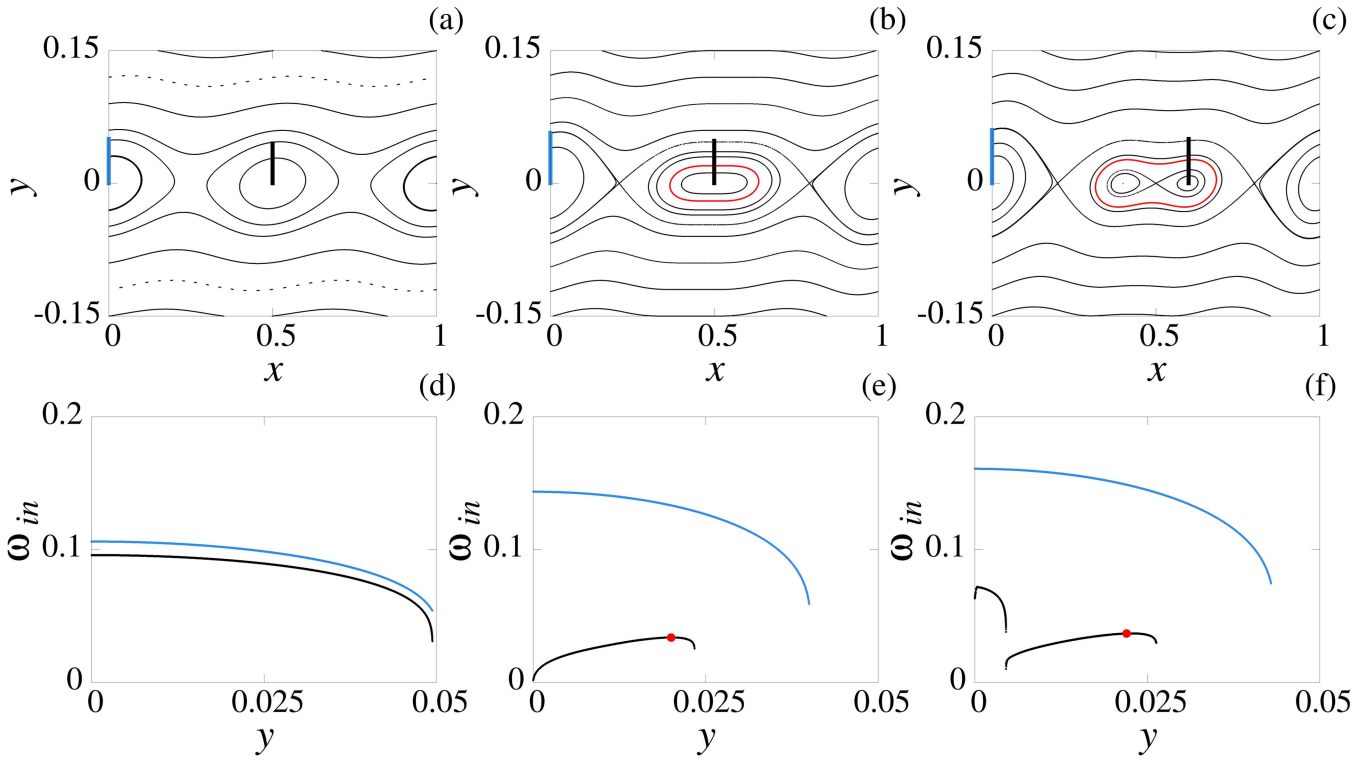

FIG. 2. Transition from mode $m_1 = 2$ to mode $m_2 = 3$ in the two-harmonic standard map. For all cases, $K_1 = 0.1$. In (a) and (b), we have the predominance of mode $m_1 = 2$, with $K_2 = 0.01$ and $K_2 = 0.1$, respectively. For $K_2 = 0.15$, we have the phase shown in (c), where the pitchfork bifurcation has already happened, and we observe three elliptic points. The internal winding number profiles for each phase space (a)–(c) are shown in panels (d)–(f), respectively. The profiles are computed in the blue and black lines presented in the phase space, and each profile corresponds to the line with the same color. The red curves and red points indicate shearless tori.

In contrast, shearless tori can exist around the elliptic point at $(x, y) = (0.5, 0)$, as evidenced by the extrema observed in the ω_{in} profiles in Figs. 2(e) and 2(f). These extreme points are marked by red circles, and the respective shearless tori are also marked in red on the phase spaces of Figs. 2(b) and 2(c). The shearless tori are identified by maxima points in the ω_{in} profiles and are located in the central region of the islands in the phase spaces. They emerge before the pitchfork bifurcation [Fig. 2(b)] and persist after it [Fig. 2(c)].

B. Emergence of multiple shearless curves

In addition to the pitchfork bifurcation, saddle-node bifurcations can also be part of the transition routes between modes. It was observed that saddle-node bifurcations occur in pairs within islands, leading to changes in their structure due to the emergence of new periodic points. As an example to study the possibility of shearless tori in these scenario, we examine the transition from mode $m_1 = 1$ to mode $m_2 = 5$. Repeating the analysis performed in Sec. II A, the phase spaces and the corresponding ω_{in} profiles are shown in Fig. 3.

In the phase spaces of Fig. 3, we observe the predominance of mode $m_1 = 1$ for all amplitudes K_1 and K_2 studied. Although the five islands associated with mode $m_2 = 5$ are not observed, we can identify the effect of the second mode by the distortion on the island of Figs. 3(b) and 3(c). However, from the results shown in Ref. 24, we know that four islands will emerge inside the large distorted island centered at $(x, y) = (0, 0)$ by four simultaneously saddle-node bifurcations.

In panels (d)–(f) of Fig. 3, we present the respective internal winding number profiles computed over the black line at $x = 0$ shown in the phase spaces of Figs. 3(a)–3(c). Similar to the first scenario presented in Figs. 2(d), the ω_{in} profiles also decrease monotonically in Fig. 3(d). However, the functions associated with these profiles differ from one another: while for Fig. 2(d), the profile resembles half of a parabola, in Fig. 3(d), the function is similar to a sum of $\sin(x)$ terms with different frequencies. Increasing the amplitude K_2 of the second mode, we have the profile shown in Fig. 3(e) with two extreme points, one maximum and one minimum, highlighted by the red points. These two points indicate the presence of two shearless curves in the phase space, and such curves are highlighted in red in Fig. 3(b). In panel (e), for y close to $y = 0.1$, the profile exhibits a shape similar to the one in panel (d), indicating a degree of similarity between the two profiles.

In the final panel, Fig. 3(f), we present the ω_{in} profile for the islands of phase space in Fig. 3(c). This case corresponds to the largest value of K_2 studied. From the winding number profile, we can identify four extreme points: two maxima and two minima. One

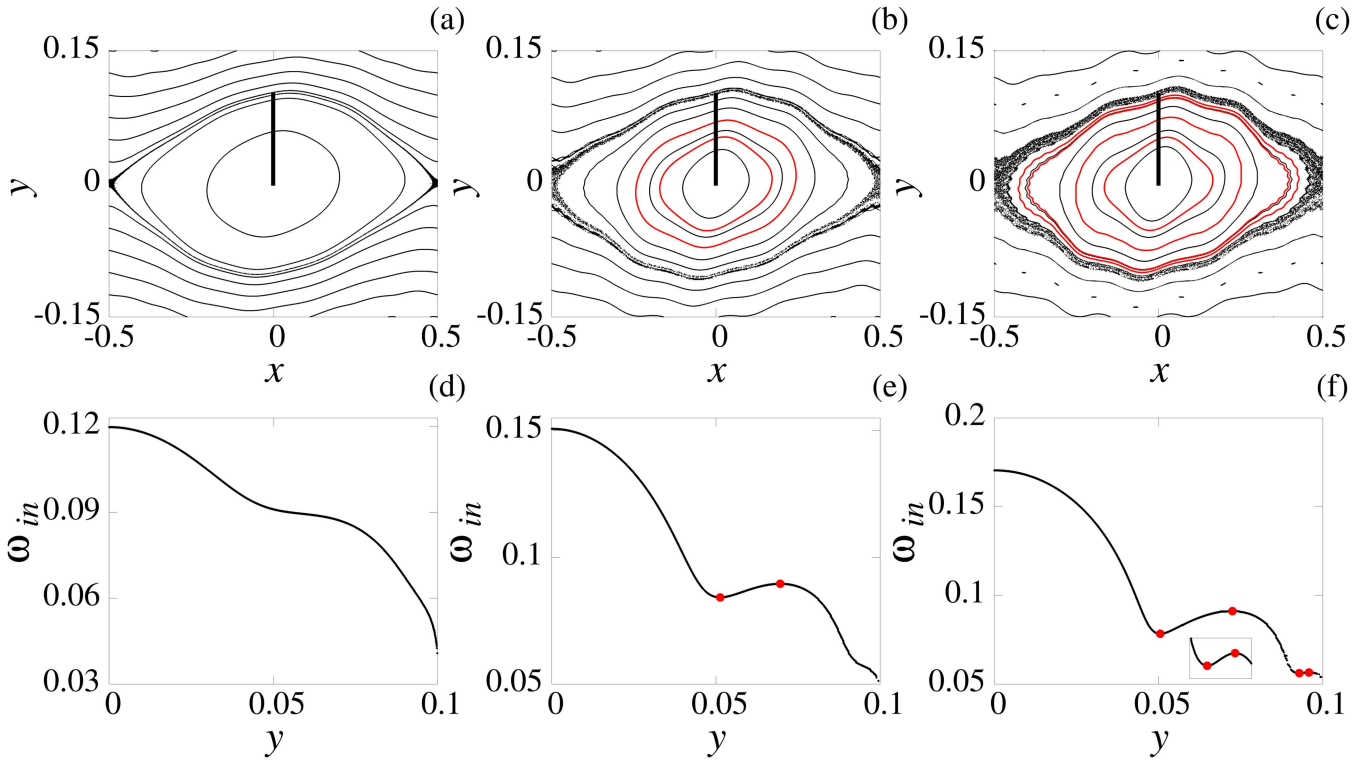

FIG. 3. Effect of the second mode $m_2 = 5$ in the first mode $m_1 = 1$ for $K_1 = 0.1$ and different amplitudes K_2. In (a), $K_2 = 0.04$, (b) $K_2 = 0.12$, and (c) $K_2 = 0.18$. For all panels, the first mode is predominant since there is only one elliptic point and is in the line $y = 0$. The action of the second mode is more noticeable in panels (b) and (c) where we observed the distortion of the islands. The red curves indicate the shearless tori. The internal winding number profiles respective to phase spaces (a)–(c) are shown in panels (d)–(f), respectively, with the extremes highlighted by the red circles, which indicate the position of the shearless curves.

pair of extrema points is the same pair as in Fig. 3(e) while the new pair emerges near $y = 0.1$, which is zoomed in the inset. The four respective twistless curves are shown in red in Fig. 3(c).

From the sequence of internal winding number profiles shown in Figs. 3(d)–3(f), we can identify a pattern in the modification of the profile and the emergence of shearless curves. First, the profile is monotonic with varying concavities and inflection points. As we increase the amplitude of the second mode, a pair of maximum–minimum points emerge in the profile, replacing an inflection point and indicating the emergence of a pair of shearless curves. This sequence can occur multiple times in the profile, with some inflection points giving rise to two shearless curves, while others remain as inflection points in the profile.

C. Emergence of shearless curves in different islands

Different isochronous islands can undergo various bifurcations as one parameter changes. Here, we investigate whether shearless curves can emerge in different islands. For this to happen, bifurcations must take place inside the islands. Thus, we choose the configuration $m_1 = 2$ and $m_2 = 5$, where pitchfork and saddle-node bifurcations occur within the two initial islands. The transition from mode $m = 2$ to $m = 5$ is shown in Figs. 4(a)–4(c). This transition involves an intermediate mode, $m = 3$, due to the pitchfork bifurcation occurring first in the island at $x = 0.5$, as we can observe in Fig. 4(b). After this first bifurcation, two elliptic points emerge inside the island centered in $x = 0$ by two saddle-node bifurcations, as shown in Fig. 4(c).

The internal winding number profiles calculated with respect to the two initial elliptic points are shown in Fig. 4(d). The black curve, related to the elliptic point at $(x, y) = (0, 0)$, monotonically decreases, while the blue curve, associated with the point at $(x, y) = (0.5, 0)$, exhibits a maximum, indicating the presence of a shearless curve.

If we increase the parameter K_2 from $K_2 = 0.05$, of Fig. 4(d), to $K_2 = 0.2$, the corresponding ω_{in} profiles are shown in Fig.4(e). In this case, both profiles exhibit extreme points, indicated by the red circles, and each profile displays different behavior. For the island centered at $x = 0$, we observe the emergence of a pair of shearless curves, where the ω_{in} profile exhibits one maximum and one minimum point, as discussed in Sec. II B. Otherwise, the blue profile, computed in relation to the elliptic point where the pitchfork bifurcation emerges, shows a maximum value (indicated by the red circle) and a cusp, indicating the separatrix passing through $x = 0.5$ within the island.

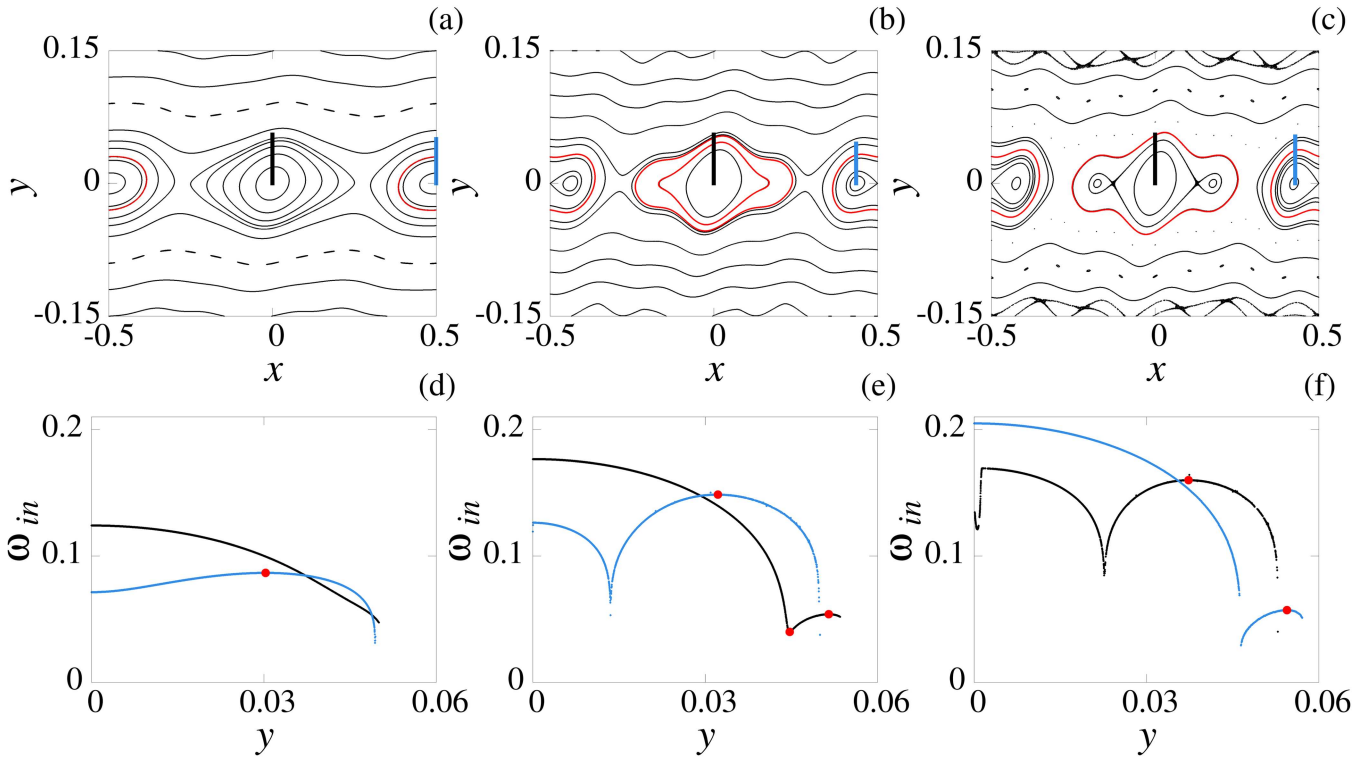

FIG. 4. Emergence of twistless torus in different islands for $m_1 = 2$ and $m_2 = 5$. For all panels $K_1 = 0.1$ and the amplitude of the second mode is (a) $K_2 = 0.05$, (b) $K_2 = 0.2$, and (c) $K_2 = 0.3$. While we observe the emergence of just one shearless torus around the elliptic point at $(x, y) = (-0.5, 0)$, we observe two curves around the point $(x, y) = (0, 0)$. The respective winding number profiles are shown in (d)–(f).

For $K_2 = 0.3$, we have the profiles shown in Fig. 4(f). In this case, one of the shearless curves around $x = 0$ has already broken and both profiles exhibit a cusp and a maximum, indicated by the red circles. Both cusps represent separatrices. Inside the pair of shearless curves in the central island, around the elliptic point at $(x, y) = (0, 0)$, two pairs of elliptic–hyperbolic points emerge via saddle-node bifurcations.

From our observations, the emergence of shearless curves precedes the bifurcations that occur at the periodic points. In addition to the shearless curves discussed in this paper, we analyze the emergence of these curves for all combinations of $m_i = 1, 2, 3, 4, 5$, and 6 for $i = 1$ and 2, and we noticed that the emergence of a single curve occurred before a pitchfork bifurcation, whereas the emergence of pairs of curves precedes saddle-node bifurcations.

III. ULLMANN'S MAP DOUBLE COUPLING

For the second system studied, we consider a symplectic mapping[31] that describes the evolution of a magnetic field line configuration capable of confining plasma along a torus. This configuration is periodically perturbed by an ergodic magnetic limiter, which is essentially a set of coils through which electric currents flow. The mapping uses radial (r) and poloidal (θ) coordinates to describe the position of a magnetic field line, analogous to cylindrical coordinates. A more detailed discussion of the relationship between the mapping and the physical system is provided in the Appendix.

The equations that describe the magnetic field line positions, at the plasma confinement equilibrium, are given by (4) and (5),

$$r^* = r, \tag{4}$$

$$\theta^* = \theta + \frac{2\pi}{Nq(r^*)}, \tag{5}$$

where N is the number of coils and $q(r)$ is the cylindrical safety factor,[32] determined by the poloidal and toroidal magnetic fields. We adopted the same safety factor as in Ref. 25.

Equations (4) and (5) define the toroidal evolution of a magnetic field line initially located at (r, θ), mapping it to the position (r^*, θ^*) after a toroidal shift of $2\pi/N$ radians, before considering the perturbation caused by the ergodic magnetic limiter. The ergodic limiter is formed by two pairs of coils, each producing a perturbation mode of type (m, n), and, between coils of the same pair, there is a poloidal twist generated by $\alpha_i = \pi n_i/m_i$, where n_i is the toroidal number of the perturbation (m_i, n_i) chosen for the system.

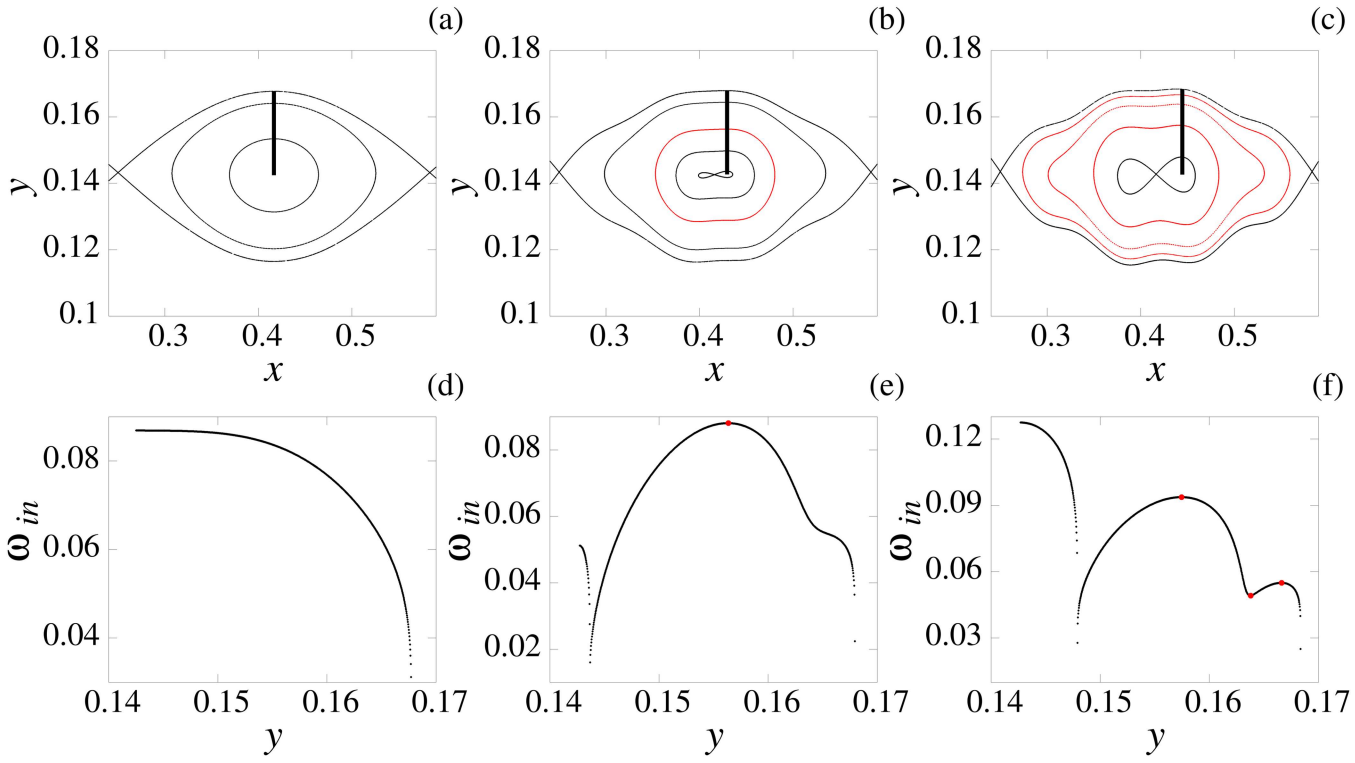

FIG. 5. Arrangement {(3, 1), (12, 4)}. The panels (a), (b), and (c) show the same island for $\epsilon_2 = 0.000\,113$, 0.001 130, and 0.004 519, with $\epsilon_1 = 0.005\,648$. Panels (d), (e), and (f) display the internal winding number profile for each case. The shearless curve emerges either alone or in a pair.

The equation

$$r^* = r + \frac{bm_iC_i}{m_i - 1}\left(\frac{r}{b}\right)^{m_i-1} \sin\left[m_i(\theta^* + (j_i - 1)\alpha_i)\right] \tag{6}$$

determines how the radial position r^* is affected by the coil j_i ($j = 1, 2$) of the pair i ($i = 1, 2$), and the coordinate r represents the field line position after the perturbation. Equation (6) determines r implicitly, requiring a numerical root-finding method for its solution. In this study, we employed the Newton–Raphson method.

The equation governing the change in θ due to the perturbation is

$$\theta = \theta^* - C_i\left(\frac{r}{b}\right)^{m_i-2} \cos\left[m_i(\theta^* + (j_i - 1)\alpha_i)\right], \tag{7}$$

where θ^*, as mentioned before, is the poloidal field line position immediately before the perturbation coil, while θ is the poloidal position after it. The parameter C_i is a dimensionless constant,

$$C_i = \frac{2\epsilon_i m_i g a^2}{q(a)R_0 b^2}, \tag{8}$$

proportional to the rate of the electric current I_i in each pair and the plasma current I_p, $\epsilon_i = I_i/I_p$, the length g of the coils, the square of the column plasma radius a, and inversely proportional to the tokamak's major radius R_0 and the square of its minor radius b.

The configuration of the ergodic magnetic limiter we adopted compels the Ullmann map to be a composition of equations of the equilibrium and the perturbation calculated four times. Consequently, there is no explicit formula linking (r_n, θ_n), the nth intersection of the field line with the Poincaré section, to the subsequent intersection (r_{n+1}, θ_{n+1}). For a single complete revolution of a magnetic field line around the torus, we compute equations (4), (5), (6), and (7), in this order, four times.

We configured the coil settings so that the same magnetic surface is perturbed by two distinct resonant modes, (m_1, n_1) and (m_2, n_2). The ratio m/n determines the perturbation of the magnetic field line with winding number $\omega = n/m$. All results presented below correspond to perturbations of the magnetic field line surface with rotational number 1/3. To enhance the visualization of the Poincaré sections, we adopted the coordinate transformation $(X = \theta/2\pi, Y = (b - r)/b)$.

A. Emergence of a single shearless curve and a pair of shearless curves

Initially, we examine the arrangement {(3, 1), (12, 4)}. The set of coils responsible for the (3, 1) resonance is kept constant at the value $\epsilon_1 = 0.005\,648$, while the second parameter, ϵ_2, is varied. The magnitude of this second parameter determines whether a chain of islands of type (12, 4) emerges.

We begin the investigation with $\epsilon_2 = 0.000\,113$. In this case, only the $(3, 1)$ island chain is present. We focus on one of the islands in this mode, specifically the island with the X coordinate in the interval $[0.2, 0.6]$, as shown in Fig. 5(a). As the value of ϵ_2 increases, bifurcations take place, and beyond a certain threshold, the system transitions into the $(12, 4)$ mode. We identify each mode by counting the number of stable (or unstable) periodic orbits of period 3 present in the system.

In Fig. 5(d), we present the winding number profile associated with the island shown in Fig. 5(a) for $\epsilon_2 = 0.000\,113$. The vertical line segment in Fig. 5(d) consists of approximately 10^3 points, each representing an initial condition that contributes to the winding number profile.

The initial profile, shown in Fig. 5(d), is monotonic. However, the subsequent case, depicted in Fig. 5(e) for $\epsilon_2 = 0.001\,130$, exhibits a non-monotonic profile with two local extrema. Only the extremum marked by a highlighted point defines a shearless curve, shown in red in Fig. 5(b). The other extremum, a local minimum, determines a separatrix that arises from the saddle-node bifurcation occurring at the center of the island, as shown in Fig. 5(b). Note that, according to the previously established method for counting bifurcations, the system is in the resonant mode $(6, 2)$.

At first glance, it may appear that a pitchfork bifurcation has occurred: the elliptical point in Fig. 5(a) transforms into a hyperbolic point in Fig. 5(b), with two elliptical points simultaneously emerging. However, what actually occurs is that the elliptical point in Fig. 5(a) shifts to the right, followed by a saddle-node bifurcation. This explains why the vertical line segment is displaced to the right relative to Fig. 5(a).

If we increase ϵ_2 further, two new shearless curves emerge, as illustrated for $\epsilon_2 = 0.004\,519$ in Fig. 5(c). These curves correspond to the second and third red curves, counted from the interior to the exterior of the island in this panel. The innermost of these two curves is associated with the minimum highlighted by a red dot in the winding number profile shown in Fig. 5(f). Upon a further increase of ϵ_2, this curve transitions into a separatrix as bifurcations occur—first defining the mode $(9, 3)$ and subsequently the final mode $(12, 4)$. Since no additional shearless curves arise for $\epsilon_2 > 0.004\,519$, we have opted not to display the stage involving all bifurcations.

B. Emergence of multiple pairs of shearless curves

We now investigate the arrangement $\{(3, 1), (15, 5)\}$ by coupling the modes $(3, 1)$ and $(15, 5)$. When the perturbation parameter ϵ_2 is varied, four bifurcations occur before the island chain $(15, 5)$ is formed. The system will pass through the modes $(6, 2)$, $(9, 3)$, and $(12, 4)$ via saddle-node bifurcations, finally achieving the mode $(15, 5)$. Each of these modes can be associated with a pair of shearless curves. However, the bifurcations are not shown since they occur for values of ϵ_2 greater than those necessary for the emergence of shearless curves.

In Fig. 6(a), we show one of the islands of the mode $(3, 1)$ when $\epsilon_2 = 0.000\,113$. The winding number profile for this perturbation value is monotonic, as shown in Fig. 6(b). Therefore, there are no shearless curves.

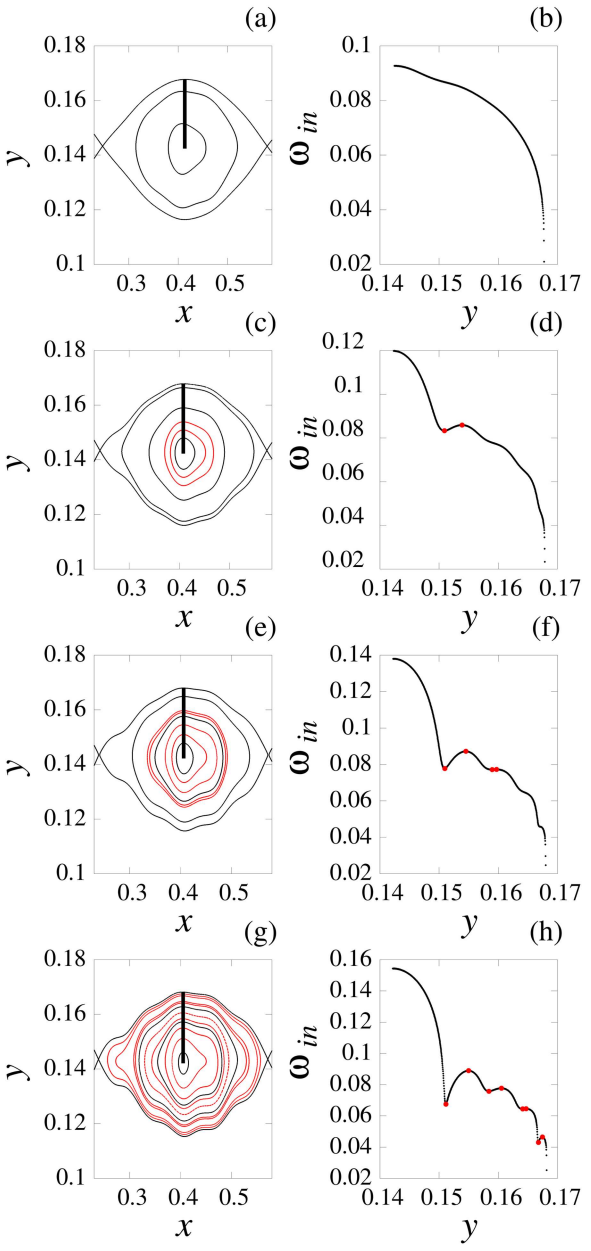

FIG. 6. Arrangement $\{(3, 1), (15, 5)\}$. Panels (a), (c), (e), and (g) show the same island for $\epsilon_2 = 0.000\,113$, $0.002\,259$, $0.003\,389$, and $0.004\,519$ with $\epsilon_1 = 0.005\,648$. Panels (b), (d), (f), and (h) display the internal winding number profile for each case. The shearless curve emerges in pairs.

Nevertheless, for $\epsilon_2 = 0.002\,259$, we observe the first pair of these curves emerging in the Poincaré section of Fig. 6(c); we have highlighted them in red. The winding number profile for this case is shown in Fig. 6(d). It contains two local extrema, corresponding to the pair of shearless curves. Along with the emergence of local extrema and the transformation of the profile into a non-monotonic

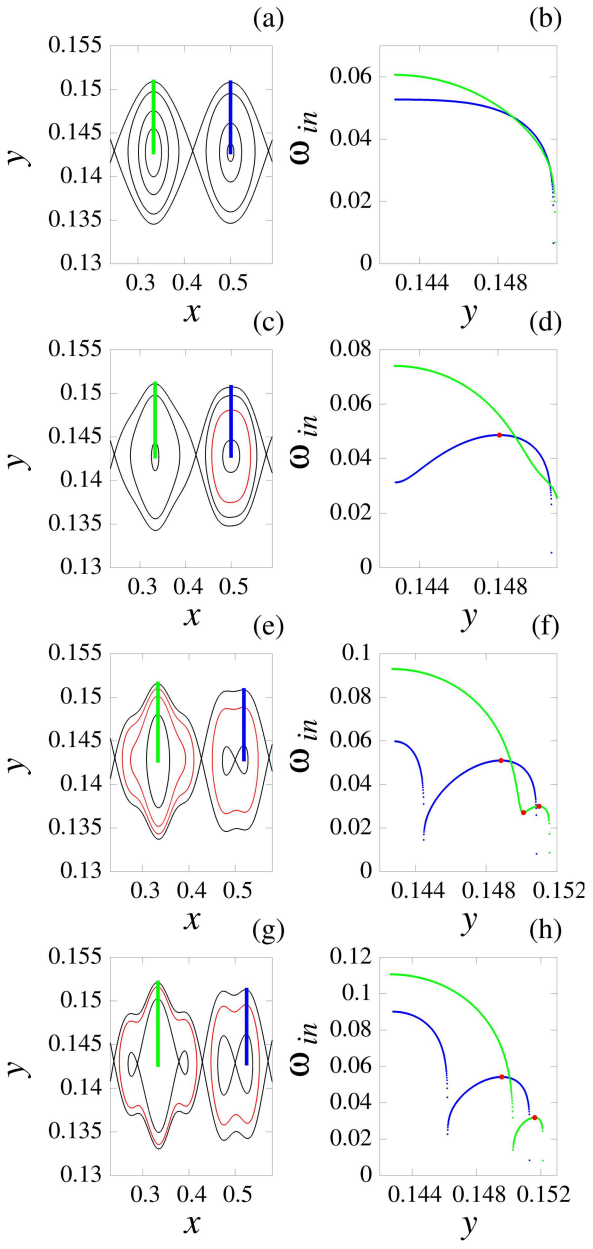

FIG. 7. Arrangement $\{(6,2),(15,5)\}$. Panels (a), (c), (e), and (g) show two islands belonging to independent chains for $\epsilon_2 = 0.000\,113$, $0.000\,565$, $0.001\,356$, and $0.002\,259$, respectively, along with their internal winding number profiles in panels (b), (d), (f), and (h). The occurrence of shearless curves differs between the chains. In all cases, $\epsilon_1 = 0.001\,130$.

form, the profile exhibits a degree of rippling. This phenomenon is visually evident in the interval $y \in [0.155, 0.165]$.

In Fig. 6(f), for $\epsilon_2 = 0.004\,519$, a second pair of extrema emerges within the interval where ripples were previously observed. These extrema are close to each other, as seen in both the corresponding profile and the associated Poincaré section in Fig. 6(e). Nevertheless, this pair of extrema (and shearless curves) will become more pronounced as ϵ_2 increases.

In the same rippled region, two additional pairs of extrema emerge. Figure 6(g) illustrates the final stage, where all shearless curves have emerged. Altogether, there are eight shearless curves, with four corresponding to local maxima and four to local minima in the winding number profile, as shown in Fig. 6(h).

As ϵ_2 continues to increase, internal island bifurcations arise, contributing to the eventual formation of the mode (15, 5). All shearless curves associated with local minima in the profiles become separatrices, and no further shearless curves are generated. In summary, the arrangement $\{(3,1),(15,5)\}$ illustrates a scenario where shearless curves appear in pairs, allowing us to assign one pair of these curves to each bifurcation.

C. Emergence of shearless curves in different islands

The final case presented with the Ullmann map is for the arrangement $\{(6,2),(15,5)\}$. It exhibits behavior similar to those observed in the previous cases. However, the number of shearless curves that appear for each island chain is different. The investigation begins at the mode (6, 2), which consists of two isochronous (3, 1) islands. Therefore, we present two islands simultaneously in Figs. 7(a), 7(c), 7(e), and 7(g). Each one of these islands belongs to one of the two (3, 1) island chains. In these four panels, we keep $\epsilon_1 = 0.001\,130$ fixed and increase ϵ_2.

In Fig. 7(a), the leftmost island has an internal winding number profile depicted in green, as illustrated in Fig. 7(b). The rightmost island has its internal winding number profile depicted in blue. Both profiles are monotonic and $\epsilon_2 = 0.000\,113$.

When $\epsilon_2 = 0.000\,565$, the green profile remains monotonic. However, the blue profile, initially monotonic in Fig. 7(b), becomes non-monotonic, as shown in Fig. 7(d). This transition is accompanied by the appearance of a shearless curve, depicted as a red curve on the largest rightmost island in Fig. 7(c). It is worth noting that the appearance of the shearless curve is identical to that shown in Fig. 5(b). Specifically, only one shearless curve appears due to a local maximum in the profile.

Eventually, the green profile also becomes non-monotonic. As shown in Fig. 7(f), it develops two local extremes—one local minimum and one local maximum—corresponding to the pair of shearless curves visible in Fig. 7(e) for $\epsilon_2 = 0.001\,356$. In this example, the arising of the shearless curves is similar to the one shown in Fig. 4(c).

However, it should be noted that the emergence of the shearless curves will not be associated with a double saddle-node bifurcation. Instead, two saddle-node bifurcations will occur at values very close to each other (the results shown in Ref. 23 suggest that the bifurcations in the Ullmann map appear one by one). Nevertheless, the number of shearless curves is identical to that observed in the case of a double bifurcation.

The bifurcations can be seen in Fig. 7(g), left island, for $\epsilon_2 = 0.002\,259$. With the bifurcations, the shearless curve determined by the local minimum in Fig. 7(f), the green profile, becomes an internal separatrix. The winding number profiles associated with this Poincaré section are depicted in Fig. 7(h), where only the shearless curves determined by local maxima persist.

IV. WALKER–FORD HAMILTONIAN

Complementary to the discrete maps shown so far, we also included a Hamiltonian flow as an alternative framework for the bifurcations and the emergence of shearless invariants. The Hamiltonian model in question was initially meant to describe the two-dimensional dynamics of a star moving around a galaxy center with a cylindrical symmetric potential. It was first used to numerically prove the emergence of chaos due to the lack of a third integral of motion when perturbations acted on the system.[33]

In an action-angle format, its non-perturbed (hence integrable) form reads

$$H_0(J_1, J_2) = J_1 + J_2 - J_1^2 - 3J_1J_2 + J_2^2 \tag{9}$$

for J_1 and J_2 as action variables. From this point on, Walker and Ford consider two coupled oscillators to simulate the effects of single and double resonances on the appearance of stability islands in phase space.[26,29] Thus, the complete Hamiltonian considers the non-perturbed term H_0 and two controlled perturbations,

$$H(\theta_1, \theta_2, J_1, J_2) = H_0 + H_1 + H_2, \tag{10}$$

with each perturbation mode as

$$\begin{aligned} H_1(\theta_1, \theta_2, J_1, J_2) &= \alpha J_1 J_2 \cos(m\theta_1 - n\theta_2), \\ H_2(\theta_1, \theta_2, J_1, J_2) &= \beta J_1 J_2^{\frac{3}{2}} \cos(r\theta_1 - s\theta_2), \end{aligned} \tag{11}$$

where (m, n) and (r, s) are the modes controlling the amount of islands generated by H_1 and H_2, respectively. The amplitudes α and β control their size.

The phase space analysis in this case takes place for a discrete map generated by the intersection of the flow trajectories with a surface section—here taken as $(\theta_1 = \frac{3\pi}{2})$. In general, we still have a resonance between modes, although now corresponding to oscillatory terms in the energy function (i.e., the Hamiltonian itself in the present model).

For the purpose of this work, we fixed the amplitude and mode of H_1 to $\alpha = 0.02$ and $(m, n) = (2, 2)$, focusing on the effect of the second perturbation H_2 as its amplitude and modes change. This limitation of equal mode numbers is meant to reduce the dynamics in phase space, so as to isolate and reproduce the same scenarios seen for the two-harmonic standard map and Ullmann's map. Moreover, in this arrangement, since resonance modes are multiples of each other, no chaos is generated, as it is always possible to define a single angle variable $\Theta = \theta_1 - \theta_2$, reducing Hamiltonian (10) to a one-degree-of-freedom system with H as constant of motion (given its explicit time independence). However, non-multiple modes are enough to induce chaos in the system if desired.

A. Emergence of one shearless curve

Primarily, in the absence of the second perturbative mode (when $\beta = 0$), phase space presents isolated islands in a period-two

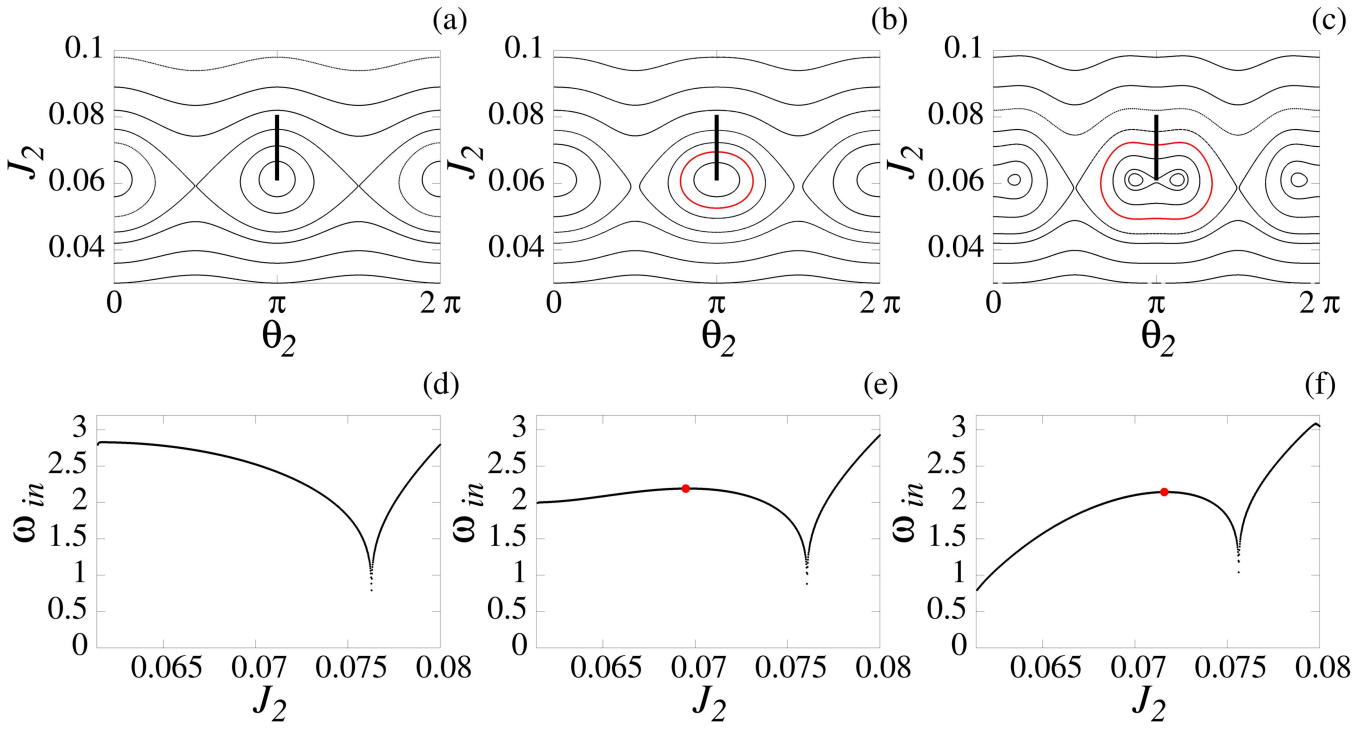

FIG. 8. Arrangement {(2, 2), (4, 4)}. Panels (a), (b), and (c) show $\beta = 0.0$, 0.01, and 0.02, respectively. The corresponding winding number profile ω_{in} is shown below each frame, *i.e.* (d), (e), and (f). In all cases, $\alpha = 0.02$, $H = 0.22$.

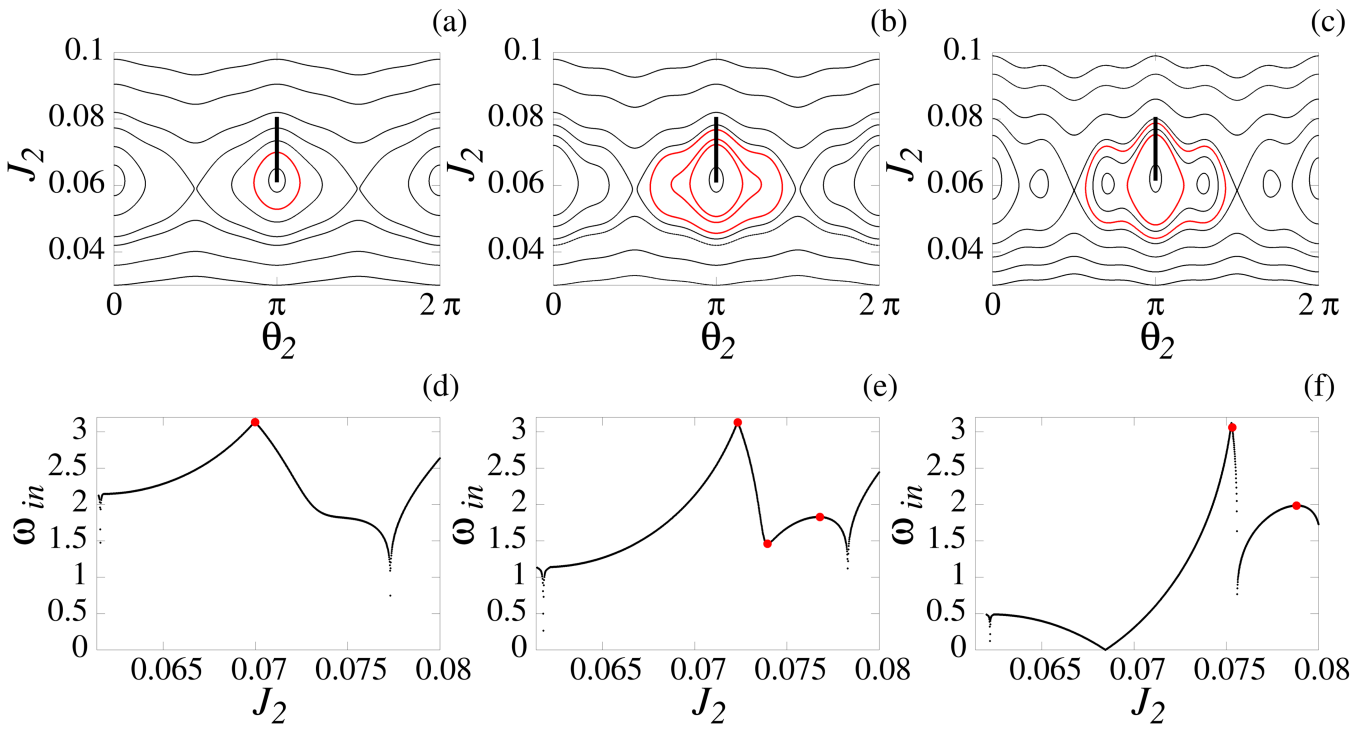

FIG. 9. Arrangement $\{(2,2),(6,6)\}$. Panels (a), (b), and (c) show $\beta = 0.01, 0.02$, and 0.04, respectively. The corresponding winding number profile ω_{in} is shown below each frame, *i.e.* (d)–(f). In all cases, $\alpha = 0.02$, $H = 0.22$.

chain, as generated by the (m,n) mode [Fig. 8(a)] with a monotonic winding number profile [Fig. 8(d)]. As soon as the second mode is introduced, both islands maintain their internal structure without a bifurcation for $\beta < 0.02$ [Fig. 8(b)], although with a winding profile presenting a slight plateau [Fig. 8(e)].

For further increasing $\beta \geq 0.02$, the second mode resonates with the first and induces a pitchfork bifurcation in both island centers independently, thereby generating a period-two chain with inner resonances also of period two [Fig. 8(c)]. These resonances increase in size with β, but without further bifurcations or emergence of extremant points in the rotation number profile. Despite inducing both phenomena, the shearless curve and the bifurcation, they are not simultaneous in this simplest case. This scenario corresponds to the same seen in Fig. 2.

B. Emergence of multiple shearless curves

When changing the perturbation mode to $r = s = 6$, for low amplitude [$\beta = 0.01$—Fig. 9(a)], the island structure is still similar to cases (a) and (b) for $r = s = 4$, but with a winding profile presenting a maximum point and two inflections [near $J_2 = 0.075$—Fig. 9(d)]. At slightly higher $\beta = 0.02$, these inflection points shift and become a minimum–maximum pair [Fig. 9(e)], therefore creating two extra shearless curves within the central island [Fig. 9(b)], although with no bifurcation occurring.

This process is roughly the same seen from Figs. 3(d) to 3(e) and 3(e) to 3(f), Figs. 4(d) to 4(e), and in Figs. 5(e) to 5(f) . At $\beta = 0.04$, the previous minimum point pinches down in the winding profile [Fig. 9(f)], forming a pit. In phase space, the previously shearless curve related to this minimum becomes the separatrix of the new islands bifurcated around the central elliptical point. The two previous maxima remain, each one forming an inner and outer shearless invariant [Fig. 9(c)].

The comparison between the simplest mode $r = s = 4$ with $r = s = 6$ suggests that the number of extremes in the winding profile increases with the period of the second perturbation and therewith the presence of shearless invariants.

One may note a minimum point in Fig. 9(f) around $J_2 = 0.068$ resembling a "cusp," as normally seen whenever winding number profiles cross a separatrix curve between islands. However, despite presenting a discontinuous derivative ($\partial\omega_{in}/\partial J_2$), it remains finite. At the same time, it does not correlate with any new structure (separatrix or island) in phase space [Fig. 9(c)] or when looking at its trajectory. This raises the doubt of whether this would be a regular shearless barrier as the ones previously discussed.

Indeed, when further investigating the emergence of this "cusp," it is seen to appear for $\beta \approx 0.032$ (all other parameters kept as in Fig. 9), exactly on the elliptic point of the island used as reference (i.e., $\theta_2 = \pi$ and $J_2 \approx 0.06$). That is, the vicinity of the island center presents a winding number close to zero. As β increases, the "cusp" position (i.e., the J_2 value for which $\omega_{in} = 0$) increases

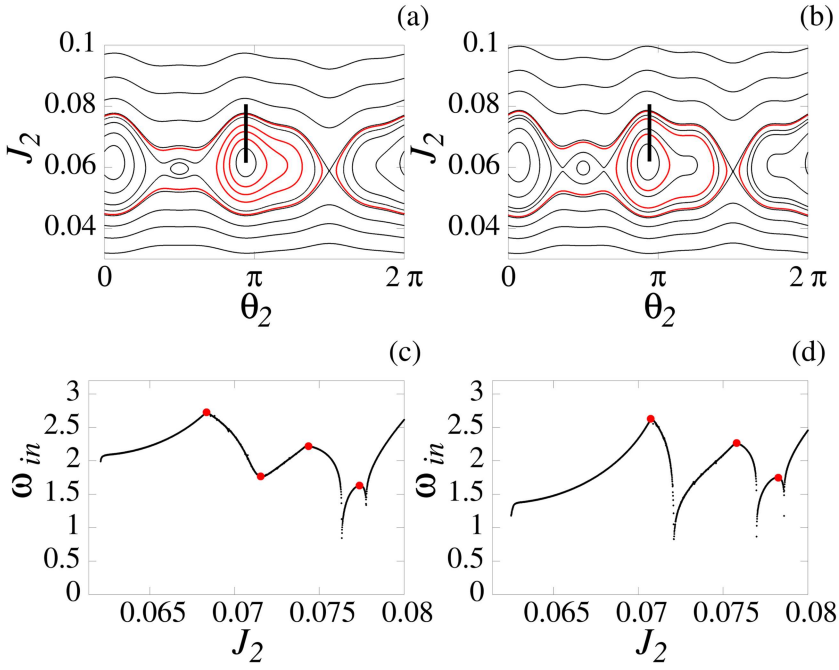

FIG. 10. Arrangement {(2, 2), (5, 5)}. Panels (a) and (b) show $\beta = 0.02$ and 0.03, respectively. The corresponding winding number profile ω_{in} is shown below each frame, i.e., (c) and (d). In all cases, $\alpha = 0.02$, $H = 0.22$.

as well, moving apart from the island center as seen in Fig. 9(c). The same phenomenon can be found for the mode $m = n = 2$ and $r = s = 5$. Therefore, the nature of the point is likely to be closer to that of a minimum that could be associated with a regular shearless curve, although originating from a different bifurcation process than the ones analyzed along the paper. For this reason, we refrain from analyzing it in more detail but find it worth mentioning.

C. Emergence of shearless curves in different islands

At last, the two scenarios shown so far correspond to resonance parameters m, n, r, and s as multiples and even numbers. This implies that resonances promote bifurcations near or over the elliptical central points, as they have similar parity. To complement these results, we also present the bifurcation behavior for an odd perturbation mode; that is, $r = s = 5$.

As shown in Fig. 10, most features are similar to what was seen for even (r, s), with the minimum point at $J_2 = 0.0715$ pinching down, while its corresponding shearless invariant becomes the separatrix of the new side island on its right [Figs. 10(b) and 10(d)]. On the other hand, given the distribution of the bifurcated islands, with elliptical center at $\theta_2 = \pi/2$ and side island at $\theta_2 \approx \pi + \pi/10$, the shearless curve extends all over the island chain, whereas the inner one remains within the previous central island.

V. CONCLUSIONS

The onset of secondary shearless curves has been previously reported in a few twist systems. In this article, we present further examples where we identify the presence of such curves in different coupled systems. Our results indicate that secondary shearless curves are commonly observed in twist systems.

By employing the two-harmonic standard map, a conservative map, we were able to discern three patterns for the emergence of shearless curves. As the perturbation parameter increases, a single shearless curve, defined by a local maximum point in the internal rotation number profile, emerges and characterizes one of the patterns. A second pattern is the emergence of shearless curves in pairs. These curves manifest as maximum and minimum pairs in the internal rotation profile. Ultimately, the shearless curve defined by the local minimum point will evolve into a separatrix in scenarios where the bifurcations are of the saddle-node type. Finally, a third pattern is observed, and pairs of shearless curves precede a double saddle-node bifurcation.

In addition to the standard map, we made use of another conservative map, which describes magnetic field lines for confinement of plasma in toroidal geometries. For this system, we were also able to identify the three patterns of the emergence of shearless curves discussed in the previous paragraph. The only difference being that shearless curves precedes only saddle-nodes and they emerge one by one.

In addition to discrete systems, we use a Hamiltonian flow, specifically the Walker–Ford Hamiltonian, to show the emergence of shearless curves in pairs, or alone, as observed on the previously studied maps. Preceding a pitchfork bifurcation, a single shearless curve appears, as defined by the emergence of a maximum in the rotation number profile. Furthermore, saddle-node bifurcations give rise to pairs of shearless curves, in accordance with the pairs of maxima and minima in the rotation profile. Nevertheless, for the Hamiltonian flow, new phenomena were also observed when compared to the discrete maps. The emergence of a shearless curve apparently without the subsequent appearance of a bifurcation and the inversion of the local maximum by a minimum in the

winding number profile together with the appearance of a new pair of shearless curves.

In summary, we numerically identified the occurrence of shearless curves in discrete and continuous twist Hamiltonian systems with the coupling of resonant modes. We noticed that the curves can appear either alone, or in pairs, and usually preceding fixed point bifurcations. When appearing in maximum–minimum pairs, the curves determined by the local minimum in the rotation profile eventually become separatrices.

ACKNOWLEDGMENTS

This research received the support of the Coordination for the Improvement of Higher Education Personnel (CAPES) under Grant Nos. 88887.320059/2019-00 and 88881.143103/2017-01, the National Council for Scientific and Technological Development (CNPq—Grant Nos. 403120/2021-7 and 311168/2020-5, 301019/2019-3), the Fundação de Amparo à Pesquisa do Estado de São Paulo (FAPESP) under Grant Nos. 2022/12736-0, 2018/03211-6, and 2023/10521-0, and CNEN (Comissão Nacional de Energia Nuclear) under Grant No. 01341.001299/2021-54.

AUTHOR DECLARATIONS

Conflict of Interest

The authors have no conflicts to disclose.

Author Contributions

B. B. Leal: Conceptualization (equal); Data curation (equal); Formal analysis (equal); Funding acquisition (equal); Investigation (equal); Methodology (equal); Validation (equal); Visualization (equal); Writing – original draft (equal); Writing – review & editing (equal). **M. J. Lazarotto:** Conceptualization (equal); Data curation (equal); Formal analysis (equal); Funding acquisition (equal); Investigation (equal); Methodology (equal); Validation (equal); Visualization (equal); Writing – original draft (equal); Writing – review & editing (equal). **M. Mugnaine:** Conceptualization (equal); Data curation (equal); Formal analysis (equal); Funding acquisition (equal); Investigation (equal); Methodology (equal); Validation (equal); Visualization (equal); Writing – original draft (equal); Writing – review & editing (equal). **A. M. Ozorio de Almeida:** Conceptualization (equal); Data curation (equal); Formal analysis (equal); Funding acquisition (equal); Investigation (equal); Methodology (equal); Validation (equal); Visualization (equal); Writing – original draft (equal); Writing – review & editing (equal). **R. L. Viana:** Conceptualization (equal); Data curation (equal); Formal analysis (equal); Funding acquisition (equal); Investigation (equal); Methodology (equal); Validation (equal); Visualization (equal); Writing – original draft (equal); Writing – review & editing (equal). **I. L. Caldas:** Conceptualization (equal); Data curation (equal); Formal analysis (equal); Funding acquisition (equal); Investigation (equal); Methodology (equal); Validation (equal); Visualization (equal); Writing – original draft (equal); Writing – review & editing (equal).

DATA AVAILABILITY

The data that support the findings of this study are available from the corresponding author upon reasonable request.

APPENDIX: ULLMANN'S MAP FOR MULTIPLE RESONANCES

In the context of magnetic confinement plasma, with the ultimate goal of achieving power fusion, there are a number of confinement settings that employ a magnetic perturbation. The primary objective of such a perturbation is to generate a chaotic magnetic layer that mitigates certain types of instabilities or allows the escape of the magnetic lines in a suitable manner. Some examples of these devices are the divertor,[32] saddle coils as in DIII-D,[34] and the magnetic ergodic limiter.[35]

The symplectic mapping[31] given by Eqs. (4)–(7) describes the evolution of a magnetic field line configuration capable of confining a plasma along a torus. The model, as determined by the mapping, adopts a magnetic field of equilibrium $\mathbf{B}_{\mathbf{eq}}$ (composed of poloidal and toroidal components) that is periodically perturbed by an ergodic magnetic limiter, which is essentially a set of coils through which electric currents flow.

It is important to note that the periodicity occurs in a geometrical sense, not in a time sense; the entire confinement system is static. The mapping was originally proposed by Ullmann,[25] while the perturbation setup is analogous to that proposed in Leal *et al.*[23]

This mapping employs radial r and poloidal θ coordinates rather than action and angle variables to describe the position of a magnetic field line. They are analogous to cylindrical coordinates, and because we study the dynamics via a plane that transversely intersects the torus, there is no need for the toroidal coordinate ϕ. By construction, the Poincaré section must be located adjacent to one of the coils. As discussed before, the equations that describe the magnetic field line positions, at the plasma confinement equilibrium, are given by (4) and (5).

Equations (4) and (5) describe the toroidal evolution of a magnetic field line that has previously been localized at (r,θ) to a position (r^*,θ^*) after a $2\pi/N$ radian toroidal shift. The magnetic field line at (r^*,θ^*) is always placed after a toroidal evolution of $2\pi/N$ radian and before the perturbation due to the ergodic magnetic limiter, and the position (r,θ) is always the magnetic position line after the perturbation. For convenience, we adopted a cylindrical approximation because it reduces the emergence of chaotic field lines. Thus, the torus is approximated by a periodic cylinder of length $2\pi R$, and the equations (4) and (5) can be deduced from $\mathbf{B}_{\mathbf{eq}.} \times d\mathbf{l} = \mathbf{0}$, where $d\mathbf{l}$ is an infinitesimal segment of the field line.

Equation (5) includes $q(r)$, the safety factor, an important measure in plasma confinement in tokamaks. For example, a tokamak must operate with values of $q > 1$ to prevent kink mode instabilities. It is defined as the mean value of the ratio of the toroidal variation $\Delta\phi$ to the poloidal variation $\Delta\theta$, $\nu \equiv \Delta\phi/\Delta\theta$,

$$q \equiv \frac{1}{2\pi}\int \nu d\theta, \tag{A1}$$

and it has a simple relation with the winding number, with one being the inverse of the other: $\omega = 1/q$.

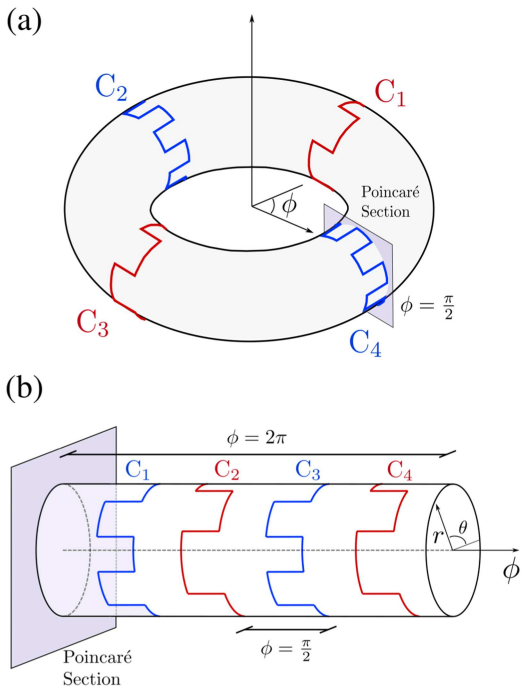

FIG. 11. (a) The magnetic coils along the toroidal chamber are equally separated from each other. In (b), the cylindrical approach is illustrated. The toroid is viewed as a 2π R-periodic cylinder.

The magnetic field line in equilibrium is perturbed by a magnetic field, whose mapping is given by equations (6) and (7). This perturbation is generated by a set of coils called an ergodic magnetic limiter. These coils produce resonances on magnetic field surface lines with a rational internal winding number. The set of coils consists of two pairs, each of which produces a mode perturbation of type (m, n). The distance between each coil of one pair is equal to π radians, and the toroidal displacement between a given coil and its neighbor is $\pi/2$ radians. In Fig. 11(a), we show an illustration of how the magnetic coils are distributed along the toroidal chamber, while Fig. 11(b) represents the cylindrical approach.

As previously mentioned, each coil pair i generates a resonance of type (m_i, n_i). To achieve this, it is necessary for each coil to have a poloidal twist relative to its counterpart. Consequently, the parameter $\alpha_i = \pi \frac{n_i}{m_i}$ must be included as a phase in the trigonometric functions of the perturbation map (6, 7).

The equations (6) and (7) are the same as those used in the work of Ref. 23 and are a version of Ullmann's map.[25] The parameter b is the minor radius of the tokamak. The poloidal mode m is the number of pairs of toroidal wire segments[35] (thus producing chains of m islands).

REFERENCES

[1] G. M. Zaslavsky, *Hamiltonian Chaos and Fractional Dynamics* (Oxford University Press, New York, 2005).
[2] A. J. Lichtenberg and M. A. Lieberman, *Regular and Stochastic Motion* (Springer Science & Business Media, 2013), Vol. 38.
[3] R. S. MacKay and J. D. Meiss, *Hamiltonian Dynamical Systems: a Reprint Selection* (CRC Press, 2020).
[4] A. Wurm, A. Apte, K. Fuchss, and P. Morrison, "Meanders and reconnection–collision sequences in the standard nontwist map," Chaos **15**, 023108 (2005).
[5] L. E. Reichl, *Transition to Chaos* (Springer, 2021).
[6] D. del Castillo-Negrete, J. M. Greene, and P. J. Morrison, "Area preserving nontwist maps: Periodic orbits and transition to chaos," Phys. D **91**, 1–23 (1996).
[7] D. del Castillo-Negrete and P. J. Morrison, "Chaotic transport by Rossby waves in shear flow," Phys. Fluids A **5**, 948–965 (1993).
[8] J. E. Howard and S. M. Hohs, "Stochasticity and reconnection in Hamiltonian systems," Phys. Rev. A **29**, 418 (1984).
[9] A. Delshams and R. De La Llave, "Kam theory and a partial justification of Greene's criterion for nontwist maps," SIAM J. Math. Anal. **31**, 1235–1269 (2000).
[10] A. Apte, A. Wurm, and P. J. Morrison, "Renormalization for breakup of invariant tori," Phys. D **200**, 47–59 (2005).
[11] R. P. Behringer, S. D. Meyers, and H. L. Swinney, "Chaos and mixing in a geostrophic flow," Phys. Fluids A **3**, 1243–1249 (1991).
[12] D. del Castillo-Negrete and P. Morrison, "Hamiltonian chaos and transport in quasigeostrophic flows," Technical Report, Institute for Fusion Studies, Texas University, Austin, TX, 1992.
[13] F. A. Marcus, T. Kroetz, M. Roberto, I. L. Caldas, E. Da Silva, R. Viana, and Z. O. Guimarães-Filho, "Chaotic transport in reversed shear tokamaks," Nucl. Fusion **48**, 024018 (2008).
[14] F. A. Marcus, I. L. Caldas, Z. O. Guimarães-Filho, P. J. Morrison, W. Horton, Y. K. Kuznetsov, and I. C. Nascimento, "Reduction of chaotic particle transport driven by drift waves in sheared flows," Phys. Plasmas **15**, 112304 (2008).
[15] D. L. Toufen, Z. O. Guimarães-Filho, I. L. Caldas, F. A. Marcus, and K. W. Gentle, "Turbulence driven particle transport in Texas Helimak," Phys. Plasmas **19**, 012307 (2012).
[16] I. L. Caldas, R. L. Viana, C. V. Abud, J. C. D. Fonseca, Z. O. Guimarães Filho, T. Kroetz, F. A. Marcus, A. B. Schelin, J. D. Szezech, D. L. Toufen *et al.*, "Shearless transport barriers in magnetically confined plasmas," Plasma Phys. Control. Fusion **54**, 124035 (2012).
[17] D. del Castillo-Negrete, "Chaotic transport in zonal flows in analogous geophysical and plasma systems," Phys. Plasmas **7**, 1702–1711 (2000).
[18] P. J. Morrison, "Magnetic field lines, Hamiltonian dynamics, and nontwist systems," Phys. Plasmas **7**, 2279–2289 (2000).
[19] H. R. Dullin, J. D. Meiss, and D. Sterling, "Generic twistless bifurcations," Nonlinearity **13**, 203 (2000).
[20] C. V. Abud and I. L. Caldas, "Secondary nontwist phenomena in area-preserving maps," Chaos **22**, 033142 (2012).
[21] C. V. Abud and I. L. Caldas, "Onset of shearless magnetic surfaces in tokamaks," Nucl. Fusion **54**, 064010 (2014).
[22] M. J. Lazarotto, I. L. Caldas, and Y. Elskens, "Island myriads in periodic potentials," Chaos **34**, 033115 (2024).
[23] B. B. Leal, I. L. Caldas, M. C. de Sousa, R. L. Viana, and A. M. Ozorio de Almeida, "Isochronous island bifurcations driven by resonant magnetic perturbations in tokamaks," Phys. Rev. E **109**, 014230 (2024).
[24] M. Mugnaine, B. B. Leal, A. M. Ozorio de Almeida, R. L. Viana, and I. L. Caldas, "Isochronous bifurcations in a two-parameter twist map," arXiv:2312.12552 (2023).
[25] K. Ullmann and I. L. Caldas, "A symplectic mapping for the ergodic magnetic limiter and its dynamical analysis," Chaos, Solitons Fractals **11**, 2129–2140 (2000).
[26] G. H. Walker and J. Ford, "Amplitude instability and ergodic behavior for conservative nonlinear oscillator systems," Phys. Rev. **188**, 416–432 (1969).
[27] J. M. Greene, H. Johannesson, B. Schaub, and H. Suhl, "Scaling anomaly at the critical transition of an incommensurate structure," Phys. Rev. A **36**, 5858 (1987).
[28] H. Johannesson, B. Schaub, and H. Suhl, "Critical exponents for an incommensurate structure with several length scales," Phys. Rev. B **37**, 9625 (1988).
[29] M. C. de Sousa, I. L. Caldas, A. M. Ozorio de Almeida, F. B. Rizzato, and R. Pakter, "Alternate islands of multiple isochronous chains in wave-particle interactions," Phys. Rev. E **88**, 064901 (2013).

[30]C. V. Abud and I. L. Caldas, "Onset of shearless magnetic surfaces in tokamaks," Nucl. Fusion.**54**, 7pp (2014).
[31]E. Ott, *Chaos in Dynamical Systems* (Cambridge University Press, 2002).
[32]J. Wesson, *Tokamaks* (Clarendon Press, 2004).
[33]M. Henon and C. Heiles, "The applicability of the third integral of motion: Some numerical experiments," Astron. J. **69**, 73–79 (1964).
[34]S. Abdullaev *et al.*, "*Magnetic Stochasticity in Magnetically Confined Fusion Plasmas*, Springer Series on Atomic, Optical, and Plasma Physics (Springer, 2014), Vol. 78, p. 412.
[35]C. J. A. Pires, E. A. O. Saettone, M. Y. Kucinski, A. Vannucci, and R. L. Viana, "Magnetic field structure in the TCABR tokamak due to ergodic limiters with a non-uniform current distribution: Theoretical and experimental results," Plasma Phys. Control. Fusion **47**, 1609 (2005).